AFRL-AFOSR-VA-TR-2019-0307

Density Functional Theory Studies of Hydrogen/Nitrogen Super-Saturation Mechanisms in Transition Metals and Metal Hydrides/Nitrides

Jennifer Wilcox
COLORADO SCHOOL OF MINES

10/29/2019
Final Report

Air Force Research Laboratory
AF Office Of Scientific Research (AFOSR)/ RTB1
Arlington, Virginia 22203
Air Force Materiel Command

REPORT DOCUMENTATION PAGE

Form Approved
OMB No. 0704-0188

1. REPORT DATE *(DD-MM-YYYY)*	2. REPORT TYPE	3. DATES COVERED *(From - To)*
10/24/2019	Final report	08/01/2016 - 07/31/2019

4. TITLE AND SUBTITLE

DENSITY FUNCTIONAL THEORY STUDIES OF HYDROGEN/ NITROGEN SUPERSATURATION MECHANISMS IN TRANSITION METALS AND METAL HYDRIDES/NITRITES

5a. CONTRACT NUMBER

5b. GRANT NUMBER

FA9550-16-1-0357

5c. PROGRAM ELEMENT NUMBER

6. AUTHOR(S)

GOMEZ-GUALDRON, DIEGO, A

5d. PROJECT NUMBER

5e. TASK NUMBER

5f. WORK UNIT NUMBER

7. PERFORMING ORGANIZATION NAME(S) AND ADDRESS(ES)

Colorado School of Mines
Chemical and Biological Engineering Department
1613 Illinois St, Golden CO 80401

8. PERFORMING ORGANIZATION REPORT NUMBER

9. SPONSORING/MONITORING AGENCY NAME(S) AND ADDRESS(ES)

AIR FORCE OF SCIENTIFIC RESEARCH
875 NORTH RANDOLPH STREET
ARLINGTON, VA 22203

10. SPONSOR/MONITOR'S ACRONYM(S)

USAF, AFRL, AFOSR

11. SPONSOR/MONITOR'S REPORT NUMBER(S)

12. DISTRIBUTION/AVAILABILITY STATEMENT

Approved for Public Release. Distribution is Unlimited.

13. SUPPLEMENTARY NOTES

14. ABSTRACT

This final report summarizes insights obtained during from DFT calculations on the dissolution of atomic species (H, N) in defect-free and defected lattices of pure metals and alloys at H/N loadings spanning under- to super-saturation conditions. These insights includes i) relationships between dissolution energies and geometry, atomic composition and electronic structure of binding sites, ii) elucidation of conditions leading to nitride/hydride formation as function of alloy composition, iii) implications of dissolution energetics on solubilities, diffusivities, plasticity and mechanical properties.

15. SUBJECT TERMS

density functional theory, alloys, vacancy formation, nitrogen/hydrogen solubility, nitrogen diffusivity, hydrides, nitrides, ab initio thermodynamics, mechanical properties, separation metal membranes

16. SECURITY CLASSIFICATION OF:			17. LIMITATION OF ABSTRACT	18. NUMBER OF PAGES	19a. NAME OF RESPONSIBLE PERSON
a. REPORT	b. ABSTRACT	c. THIS PAGE			Diego A. Gomez-Gualdron
U	U	U	SAR	33	19b. TELEPHONE NUMBER *(Include area code)* (303)-384-2319

INSTRUCTIONS FOR COMPLETING SF 298

1. REPORT DATE. Full publication date, including day, month, if available. Must cite at least the year and be Year 2000 compliant, e.g. 30-06-1998; xx-06-1998; xx-xx-1998.

2. REPORT TYPE. State the type of report, such as final, technical, interim, memorandum, master's thesis, progress, quarterly, research, special, group study, etc.

3. DATE COVERED. Indicate the time during which the work was performed and the report was written, e.g., Jun 1997 - Jun 1998; 1-10 Jun 1996; May - Nov 1998; Nov 1998.

4. TITLE. Enter title and subtitle with volume number and part number, if applicable. On classified documents, enter the title classification in parentheses.

5a. CONTRACT NUMBER. Enter all contract numbers as they appear in the report, e.g. F33315-86-C-5169.

5b. GRANT NUMBER. Enter all grant numbers as they appear in the report. e.g. AFOSR-82-1234.

5c. PROGRAM ELEMENT NUMBER. Enter all program element numbers as they appear in the report, e.g. 61101A.

5e. TASK NUMBER. Enter all task numbers as they appear in the report, e.g. 05; RF0330201; T4112.

5f. WORK UNIT NUMBER. Enter all work unit numbers as they appear in the report, e.g. 001; AFAPL30480105.

6. AUTHOR(S). Enter name(s) of person(s) responsible for writing the report, performing the research, or credited with the content of the report. The form of entry is the last name, first name, middle initial, and additional qualifiers separated by commas, e.g. Smith, Richard, J, Jr.

7. PERFORMING ORGANIZATION NAME(S) AND ADDRESS(ES). Self-explanatory.

8. PERFORMING ORGANIZATION REPORT NUMBER. Enter all unique alphanumeric report numbers assigned by the performing organization, e.g. BRL-1234; AFWL-TR-85-4017-Vol-21-PT-2.

9. SPONSORING/MONITORING AGENCY NAME(S) AND ADDRESS(ES). Enter the name and address of the organization(s) financially responsible for and monitoring the work.

10. SPONSOR/MONITOR'S ACRONYM(S). Enter, if available, e.g. BRL, ARDEC, NADC.

11. SPONSOR/MONITOR'S REPORT NUMBER(S). Enter report number as assigned by the sponsoring/ monitoring agency, if available, e.g. BRL-TR-829; -215.

12. DISTRIBUTION/AVAILABILITY STATEMENT. Use agency-mandated availability statements to indicate the public availability or distribution limitations of the report. If additional limitations/ restrictions or special markings are indicated, follow agency authorization procedures, e.g. RD/FRD, PROPIN, ITAR, etc. Include copyright information.

13. SUPPLEMENTARY NOTES. Enter information not included elsewhere such as: prepared in cooperation with; translation of; report supersedes; old edition number, etc.

14. ABSTRACT. A brief (approximately 200 words) factual summary of the most significant information.

15. SUBJECT TERMS. Key words or phrases identifying major concepts in the report.

16. SECURITY CLASSIFICATION. Enter security classification in accordance with security classification regulations, e.g. U, C, S, etc. If this form contains classified information, stamp classification level on the top and bottom of this page.

17. LIMITATION OF ABSTRACT. This block must be completed to assign a distribution limitation to the abstract. Enter UU (Unclassified Unlimited) or SAR (Same as Report). An entry in this block is necessary if the abstract is to be limited.

CHEMICAL AND BIOLOGICAL ENGINEERING DEPARTMENT

Colorado School of Mines

Golden, Colorado 80401

Final report for

Grant FA9550-16-1-0357

DENSITY FUNCTIONAL THEORY STUDIES OF HYDROGEN/NITROGEN SUPER-SATURATION MECHANISMS IN TRANSITION METALS AND METAL HYDRIDES/NITRIDES

PRINCIPAL INVESTIGATOR

Prof. Diego A. Gomez-Gualdron

Email: dgomezgualdron@mines.edu

Phone: (303) 384-2319

Fax: (303) 273-3730

Submitted to: Dr Ali Sayir

AFOSR

Materials with Extreme Properties

875 North Randolph Street

Arlington, Virginia 22203

October 24, 2019

TABLE OF CONTENT

I. SUMMARY

This section describes the accomplishments obtained during the 3-year award period under Grant AF9550-16-1-0357. The overarching goals of this project was to use molecular simulations to gain insights on the diffusion and dissolution of hydrogen and nitrogen in pure, alloyed, and defected metals and their connection to material properties and supersaturation. Research activities during Year 1-2 were performed under the guidance of Prof. Jennifer Wilcox (Principal Investigator during this time), while activities during Year 3 were performed under the guidance of Prof. Diego A. Gómez-Gualdrón (current Principal Investigator and report author).

Two research lines, based on density functional theory (DFT) calculations, were pursued during this project: *i)* the study of nitrogen dissolution and diffusion in (defect-free and defected) vanadium and vanadium alloys, and its connection to nitridation and nitrogen permeability in the context of nitrogen separation membranes, and *ii)* the study of hydrogen dissolution in (defect-free and defected) palladium and palladium alloys, and its connection to material mechanical properties in the context of hydrogen separation membranes. Scientific findings for the study of nitrogen in vanadium-based systems are detailed in one publication and one submitted manuscript under review at the time of writing this report. Scientific findings for the study of hydrogen in palladium-based systems are detailed in one publication. A publication list can be found at the end of this report.

In research line “i", alloying V with Ru or Mo were first studied as a way to reduce the binding energy of N (relative to V) under the hypothesis that this would result in a desirable concomitant increase in N diffusivity (relative to V). The electronic charge of the reduced interstitial nitrogen was found as a proxy of the binding energy. However, since calculations showed that N binding is primarily controlled by the local environment at the relevant interstitial sites, it was found that significant content of the alloying element is needed to create a significant number of binding sites with reduced binding energy. Due to synthetic challenges associated with alloys with sufficient Ru/Mo content, V_xCr_y and V_{xy} alloys became the new subject of study, which presented two types of interstitial octahedral sites: V-rich and V-depleted. The binding was found to be stronger in V-rich sites consistent with a correlation between N binding strength a number of V atom at the local binding site. N binding strength at vacancies was similar or weaker than at regular interstitial sites.

Ab initio thermodynamics suggests that the combination of strong and weak binding sites mitigated the reduction in solubility arising from alloying. However, the heterogeneity of the interstitial sites generally led to higher energy barriers for N diffusion than those encountered in pure V. The exception to this observation was the $V_{0.25}Fe_{0.75}$ alloy. Based on our calculations, at 673 K and 5 bar (N2 pressure), N solubility and diffusivity in $V_{0.25Fe0.75}$ would be ~3 times smaller and ~53 times larger, respectively, than pure V. According to the solution-diffusion model, this finding indicates that a ~18-fold higher permeability would be expected for $V_{0.25}Fe_{0.75}$ relative to V. Permeability is expected to be controlled by bulk diffusion rather than by surface processes, as in all alloys we find the energy barrier for N_2 dissociation at the alloy surface to be lower than the barrier for bulk diffusion in the same alloy. The mechanical strength of V and alloys tended to increase (and eventually plateau) as nitrogen content increase in the lattice (even beyond saturation).

In research line “ii”, through calculation of hydrogen binding energies, vacancy formation energies, phase/solubility diagrams, as well as material plastic deformation and mechanical properties during

hydrogen loading/unloading in Pd and Pd_xAg_y and Pd_xAu_y alloys, we present evidence that alloying with Au and Ag suppress hydrogen-embrittlement by reducing hydrogen solubility rather than by reduction of intrinsic tendencies to form defects. Specifically, we found that alloying leads to higher vacancy stabilization and lower elastic constants upon hydrogen dissolution (even beyond saturation) than for pure Pd. Permanent plastic deformation are also more pronounced for alloyed systems, which in some cases made subsequent hydrogen loading more favorable. On the other hand, alloying also led to unfavorable hydrogen dissolution beyond 25 at. %. The reduction in solubility is strongly related to downshift of the overall metal d-band center in the alloys along with changes to the metal Pauli repulsion factor.

II METHODS

2.1. Electronic energy calculations. The primary method for first principles calculations performed in this project was plane-wave density functional theory (DFT), with calculations performed using the Vienna Ab Initio Package (VASP). Calculations were performed within the generalized gradient approximation (GGA) framework, using the exchange-correlation functional of Perdew, Burke and Ernzerhof (PBE), and the projector-augmented wave (PAW) method to describe core electrons. The basis set of plane (Bloch) waves to build the solution to the Kohn-Sham equations was defined by an energy cutoff of at least 400 eV. Convergence of calculated electronic energies within 10^{-3} eV/atom with respect to number of k-points was determined in relevant test systems and used to inform the k-point mesh size for subsequent calculations. Energy convergence with respect to k-points was accelerated by smearing around the Fermi level using the method of Methfessel and Paxton of first order. Electronic structures were typically converged within an energy tolerance of 10^{-6} eV.

2.2. Determination of local minima and transition states. Stable geometries (local minima) for the systems of interest were found by altering geometries to minimize their electronic energy and reduce forces in the system to zero. Typically, a geometry was considered to have reached a local minimum if the acting forces on all atoms fell below 10^{-3} eV/Å. Transition state geometries (saddle points) connecting two local minima were found using the climbing image variation of the nudge elastic band method (CI-NEB). In this method, a number of intermediate geometries describing the transition from one local minimum to another are collectively optimized as to find the "minimum energy pathway." Adjacent geometries along the pathway are connected through "imaginary" springs that create additional forces on the geometries. The climbing image variation ensures that, once the energy of the pathway is minimized, the highest-energy geometry corresponds to the transition state. Typically, pathways were considered minimized when all forces fell below 5 x 10^{-2} eV/Å. When needed, the vibrational frequencies for local minima and transition states were calculated using the finite displacement method. In this method, the electronic energy of the system is calculated throughout systematic displacements of the atoms and used to estimate second derivatives to build the mass-weighted Hessian matrix of the system. The vibrational frequencies are obtained from the eigenvalues of the matrix.

2.3. Electronic structure analysis. The electronic structure of the studied systems was analyzed to understand the implications of charge transfer effects and features of the band structure (e.g. d-band center) on properties of interest in the studied materials. Charge transfer was analyzed by calculating electronic charges around atom centers according to the Bader splitting formalism of the charge density. The latter was calculated once a geometry was optimized, by recalculating the electronic structure using the tetrahedron smearing method with Blochl corrections and an FFT mesh ensuring convergence of charges within 10^{-3} *e*. To calculate the density of states (DOS), the charge density of each system was used in non-self-consistent calculations with finer k-point meshes. The obtained density was then split by projecting it on the angular momentum and sites of interest. The d-band center for the metal species of interest was calculated as the first moment of the d-band DOS projected on the lattice sites occupied by the relevant metal.

2.4. Calculation of cohesive and vacancy formation energies. When calculating the energetics of processes of interest, the standard equations encountered in the literature were utilized using the electronic energies obtained from our calculations. Cohesive energies, E_{coh}, which indicate how strongly atoms within the lattice are held together were calculated as:

$$E_{coh} = \frac{E_{lattice} - \sum N_i E_i}{\sum N_i}$$

where $E_{lattice}$ is the energy of a lattice made up of various atoms of species i. N_i is the number of atoms of species i in the lattice, and E_i is the energy of an atom of species i in isolation. Formation energies, E_v, for vacancies obtained by removing an atom of species i were calculated either as:

$$E_v = (E_{lattice})_{def} + (E_i)_{bulk} - E_{lattice}$$

where $(E_{lattice})_{def}$ and $E_{lattice}$ are the energies of the lattice with and without the vacancy, respectively, and $(E_i)_{bulk}$ is the energy of the removed atom in the bulk of a lattice made up solely of atoms of species i, or as:

$$E_v = (E_{lattice})_{def} - \left(\frac{n-1}{n}\right) E_{lattice}$$

where n is the number of atoms in the lattice without vacancies. Note that the two latter equations are equivalent for pure metals but have somewhat different interpretations of the energy penalty to form the vacancy in alloys, because they differ on the interpretation of the "reservoir" for the removed atom.

2.5. Calculation of binding, reaction and activation energies. The differential binding energies, E_{bind}, characterizing the binding of an adsorbate k to a system of interest is calculated as:

$$E_{bind} = E_{sys+k} - E_{sys} - E_k$$

where E_{sys+k} is the energy of the system with the bound adsorbate, E_{sys} is the energy of the system without the bound adsorbate, and E_k is the energy of the isolated adsorbate k. In this project, systems corresponded to either bulk lattices or surface slabs. When the adsorbates were atomic species originating from diatomic molecules, the energy of the isolated adsorbate was taken as half of the energy of the diatomic molecule. Reaction energies, E_{rxn}, for processes where a system changes from one state to another were calculated as:

$$E_{rxn} = E_{final} - E_{initial}$$

where E_{final} and $E_{initial}$ are the energies of the system in the final and initial states, respectively. The corresponding activation energy, E_a, for the process was calculated as:

$$E_a = E_{TS} - E_{initial}$$

where E_{TS} is the energy of the transition state connecting the initial and final states of the system. Note that all the energies in the preceding equations presented zero-point energy (ZPE) corrections when such correction was found to be necessary.

2.6. Calculation of atomic solubilities and diffusivities. Since the materials studied in this project were investigated in the context of metal membrane applications, various estimations of atomic solubilities (S)

and diffusivities (D) were carried during the project. The importance of these properties lies in the well-known solution-diffusion model, where the permeability, α, of a species *k* through a membrane is given as:

$$\alpha_k = S_k \times D_k$$

More than the calculated permeabilities themselves, in this project we were interested in relative permeabilities (e.g. as indicated by permeability ratios). In particular, in atomic permeabilities in alloys relative to those in reference pure metals. Diffusion was considered as an Arrhenius process, where the hopping of the diffusing atom between lattice sites is a rare event and the diffusivity is given by:

$$D_k = D_{o_k} e^{-E_{a_k}/k_B T}$$

The pre-exponential factor D_o depends, among other things, on geometrical consideration of the diffusion pathways that were similar between studied alloys and reference metals. Thus, ratios between diffusivities were estimated based on the ratios of the exponential component of the equation.

Solubilities were estimated within two theoretical frameworks. In the *first framework*, the solubility of the atomic species *k*, estimated as a ratio θ_k between the number of occupied sites and the maximum number possible of binding sites is given by:

$$\theta_k = \frac{q_{k_{sol}}}{\sqrt{\frac{q_{k_{gas}}}{PV} k_B T} + q_{k_{sol}}}$$

where q_{sol} and q_{gas} are the partition functions of the species *k* in the gas phase and dissolved in the lattice, respectively. The ideal gas approximation is used to calculate q_{gas}, whereas the harmonic approximation is used to calculate q_{sol} using the vibrational frequencies. Some, among other assumptions, built into the equation above are that the binding energy for species *k* in all potentially available interstitial sites is constant independently of the distribution and number of species *k* in the lattice, and that the latter number corresponds to dilute conditions.

In the *second framework*, corresponding to standard ab initio thermodynamics, the free energy of adsorption ΔG_{ads} for various numbers and distributions of atomic species *k* in the lattice is calculated directly as:

$$\Delta G_{ads_k} = G_{M,n_k} - G_{M,0} - n_k \mu_k$$

where $G_{M,nk}$ is the free energy of the lattice with n_k number *k* species and μ_k is the chemical potential of species *k* in the gas phase. $G_{M,nk}$ was approximated as the zero-point energy corrected electronic energy, and μ_k was calculated as the zero-point corrected electronic energy plus a $\Delta\mu_{k,0(T,P)}$ term calculated based on the ideal gas partition function. These calculations were used to build "phase diagrams" illustrating the most stable solution configuration (hence solubility) at a given T and P. To find the most stable configuration, μ_k is calculated at the (T, P) condition of interest and ΔG_{ads} is calculated for all the considered lattice configurations. The configuration yielding the lowest ΔG_{ads} is chosen to appear in the phase diagram at the

particular (T, P) condition. This approach allows to consider more dramatic changes with respect to the pure metal lattice (e.g. nitride formation during N dissolution), provided the corresponding configurations are included in the calculations. Evidently, a constraint of ab-initio thermodynamics is that if a configuration is not included in the calculations, it cannot appear in the phase diagram.

2.7. Calculation of elastic constants. To evaluate the mechanical properties of the studied systems, the elastic tensor matrix was calculated based on the tensorial form of Hook's law:

$$\sigma_{ij} = \sum_{kl} C_{ijkl}\, \epsilon_{kl}$$

where σ_{ij} is the stress, ε_{kl} is the strain, C_{ijkl} is the elastic constant, and i, j, k, and l are directions in real space. Following Voigt's notation where indices are mapped as 11 → 1, 22 → 2, 33 → 3, 23 → 4, 13 → 5, 12 → 6, the elastic constants C_{mn} of the 6 x 6 matrix relating the 6-dimensional vectors $\boldsymbol{\sigma}$ and $\boldsymbol{\varepsilon}$ can be defined. Calculation of each C_{mn} was done by systematically distorting the lattice supercell in six directions and subsequently optimizing atomic positions. The electronic energies, E, associated with each distortion were used to numerically evaluate:

$$C_{mn} = \frac{\partial \sigma_m}{\partial \epsilon_n} = \frac{1}{V} \frac{\partial^2 E}{\partial \epsilon_m \partial \epsilon_n}$$

The obtained C_{mn} were used to calculate mechanical properties (e.g. bulk modulus) using standard relationships between the property of interest and elastic constants.

III ACCOMPLISHMENTS

The information described in this section is based on the publications listed at the end of the report. Therefore, for details omitted in the discussion below, we refer to the listed publications at the end of this report.

3.1. Insights on the dissolution of atomic nitrogen in V, V_xRu_y and V_xMo_y. This work was performed during Year 1, seeking to shed light on the dissolution of nitrogen in metallic BCC lattices, which is not fully understood. Indeed, although relevant to common metallurgical processes such as nitriding, nitrogen dissolution has not been studied to the extent that the dissolution of, for instance, carbon and hydrogen have been. Since the project aim was to investigate nitrogen dissolution in the context of nitrogen separation membranes, V and two potential V alloys were chosen as case studies. As nitrogen permeability depends on both solubility and diffusivity (see Section 2.6), V was chosen as a baseline material due to its high nitrogen solubility, while the alloys were explored due to their potentially enhance the low nitrogen diffusivity in V. However, diffusivities were not directly studied until Year 3.

Vanadium case. Calculations (Fig. 1) revealed octahedral (*o*) interstitial sites in the BCC V lattice as significantly more stable binding sites for N atoms than tetrahedral (*t*) sites (diffusion studies in Year 3, revealed the *t* site to be a transition state). Consistent with the electrophilic character of nitrogen, its dissolution in either site results in the oxidation of neighbor V atoms, and the corresponding reduction of nitrogen itself, more so in the *o* than in the *t* site. The V-N distance was found to play a role in charge transfer. For instance, the two "axial" and the four "equatorial" atoms making up the *o* site presented different extents of oxidation, presumably because the former are closer to the dissolved N atom than the latter. Because electrostatic interaction energy contributes to the binding energy, charge polarization, which is higher when N binds to *o* sites, contributes to the higher stability of N in the latter. Another factor that contributes to the higher binding stability in the *o* sites is their effective radius (in a hard-sphere model), which (at 0.88 Å) matches the size of the N atom (0.75 Å).

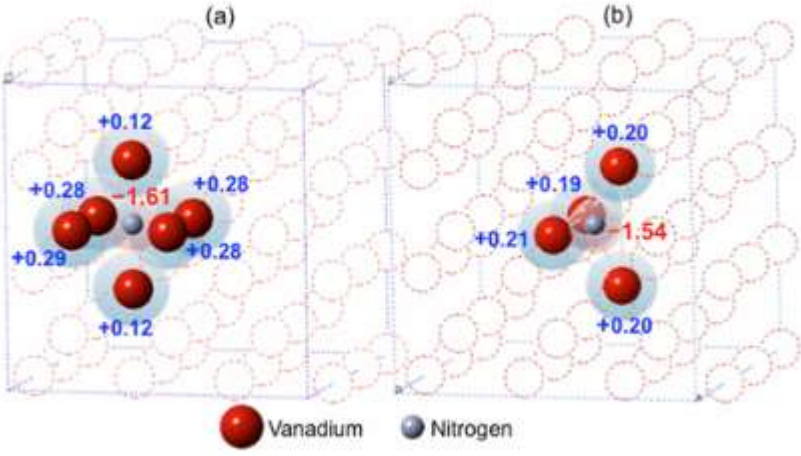

Fig. 1. Electronic charges during nitrogen dissolution in vanadium. (a) dissolution in octahedral site (E_{bind} = -2.80 eV). (b) dissolution in octahedral site (E_{bind} = -1.38 eV). [1]

Our density of states calculations (Fig. 2) reveal the chemical bonding between N and V atoms during dissolution of the former. This was evidenced by the coincidence of peaks ~6 eV below the Fermi level for

the projection of the density of d-states on N and V atoms, which suggest the existence of d-states shared by these two species, consistent with the formation of covalent bonds. The chemical bonding results in a downward shift in the d-band center of V (mostly due to axial V), which is lowered by ~0.25 eV due to the hybridization of the d-states of V and the 1π state of N. As a consequence of the chemical bonding between N and V, the lattice was observed to expand upon N atom dissolution.

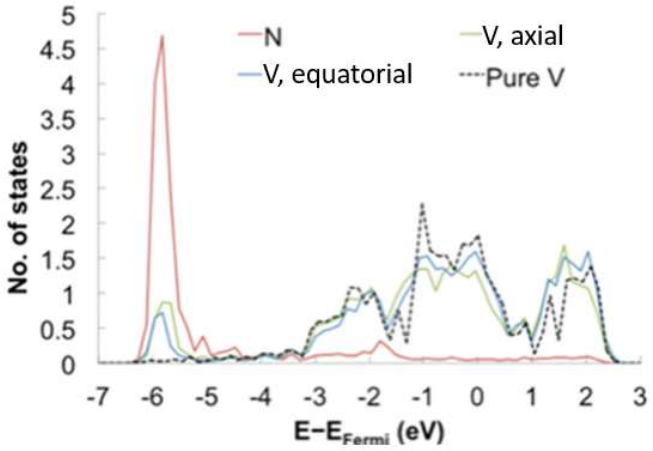

Fig. 2. Density of d-states projected on N and V atoms during dissolution. [1]

Calculations on the binding of two N atoms (e.g. Fig. 3) suggest that similar behaviors (at least qualitatively) are observed for the dissolution of multiple as for single interstitial N atoms. For instance, N atoms continue to reduce and V atoms to oxidize, and the lattice continues to expand, as more N atoms fill the lattice. However, the extent to which these phenomena occur depends entirely on the exact configuration (relative positions) of the N atoms in the lattice. N binding energies varied as much as 1.4 eV depending on the distribution of N in the lattice. Lattice volume expansion varied in the ~1.5- 3.0 % range and happened to correlate well ($R^2 \sim 0.87$) with binding energy. No clear correlation was found between binding energy and the distance between dissolved N atoms, but the closest N-N distances (from a 2.5 -5.3 Å range) do tend to result in the weakest binding energies. The lack of correlation occurs because once N-N distances are beyond 3.6 Å, binding energies oscillate around a -2.76 eV average.

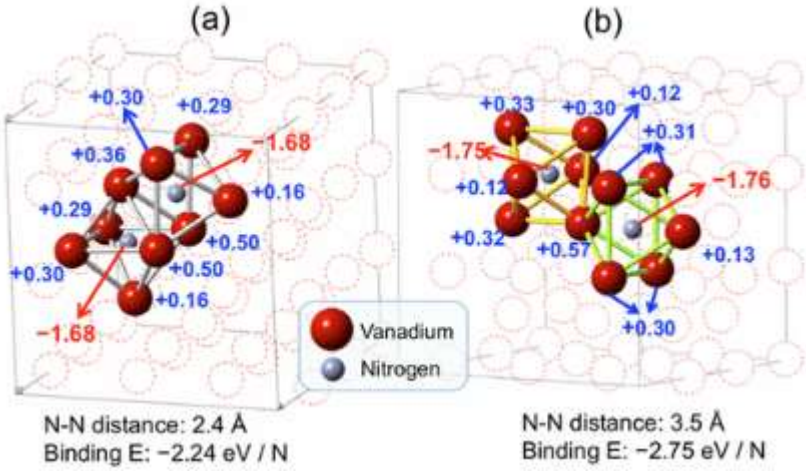

Fig. 3. Electronic charges and binding energies for two configurations illustrating multiple dissolution of N atoms in the V lattice. [1]

Vanadium-ruthenium case. Considering the well-known high permeability of H atoms in Pd membranes, one proposed material design principle to enhance N permeability in V is to reduce the N binding energy through alloying. To explore this possibility, alloys with ruthenium in the $V_{54-x}Ru_x$ (x =1-6) composition range were the first alloys investigated in this project. The Ru content was maintained low to increase the likelihood that the lattice remains BCC upon alloying (Ru is an FCC metal). The introduction of the larger Ru resulted in the following effects that in principle would weaken the binding of N: *i)* an expansion of the BCC lattice, and *ii)* a downward shift in the *d*-band center of V atoms due to hybridization with Ru *d*-states ~3.5 eV below the Fermi level (Fig. 4). However, at the studied Ru concentrations, the effects were rather weak. In particular, d-band shifts were almost inexistent for V beyond the first coordination shell around Ru.

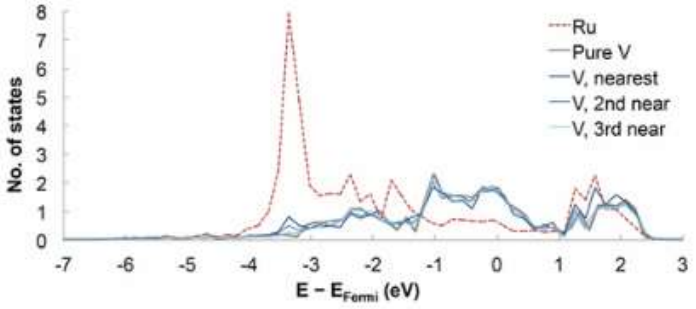

Fig. 4. Density of d-states projected on V and Ru atoms of $V_{53}Ru$ alloy. [1]

Inspection of N binding energies in different sites in $V_{54-x}Ru_x$ alloys clearly illustrated that no dramatic decreases (more than 1 eV) in the N binding energy relative to that in V occur, unless the interstitial N is in an *o* site that contains at least one Ru atom. In other words, the N binding remains essentially as strong as in pure V unless the N atom chemically bonds Ru. This is illustrated plotting the N binding energy versus the distance of the interstitial N to the nearest Ru atom in the lattice for the $V_{53}Ru$ case (Fig. 5). For $V_{54-x}Ru_x$ alloys, this became apparent by the clear correlation between N binding energy and the proportion of Ru atoms making up the *o* site.

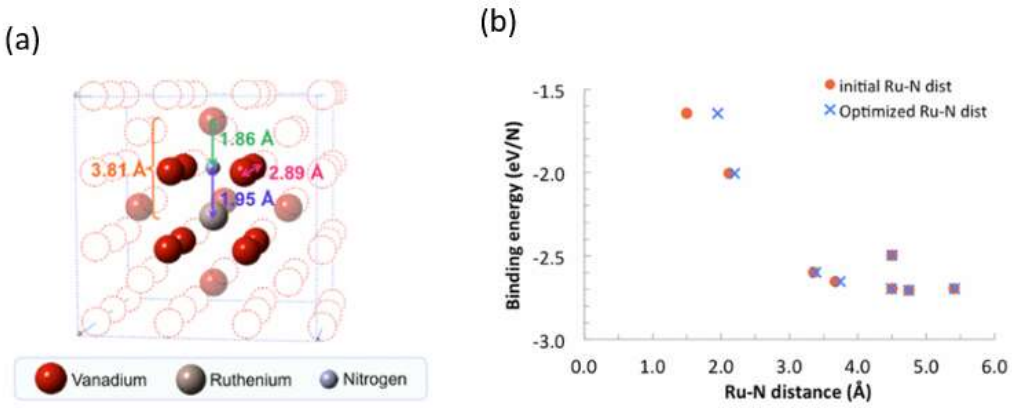

Fig. 5. Binding of a single N atom in a $V_{53}Ru$ alloy. (a) Relevant distances for interstitial N in the weakest binding site. (b) N binding energy versus distance of binding site to nearest Ru atom. [1]

The chemical bond between N and Ru when the former binds a Ru-containing *o* site is evidenced by the coincidence of peaks in the projected density of *d*-states of Ru and N ~6.2 eV below the Fermi level, suggesting the hybridization of the *d*-states of Ru and the 1π state of N (Fig. 6). The relative intensity of the peaks for the projections on Ru and V indicate the dominant role of Ru *d*-states in hybridizing the 1π state of N, even if Ru is in the minority in the *o* site. When Ru is not present in the *o* site, the 1π state of N hybridizes with V *d*-states, but at a higher position relative to the Fermi level (~5.8 eV below the Fermi level), consistent with the stronger binding energies for those cases. The higher proportion of Ru (which is significantly more electronegative than V) in the *o* site, the less the reduction of the interstitial N. Therefore, the correlation between Ru proportion in the *o* site and binding energy (which varied between -1.10 eV and 0.82 eV), engendered a correlation between the latter and the charge of the interstitial N (which varied between -1.18*e* and -1.48*e*).

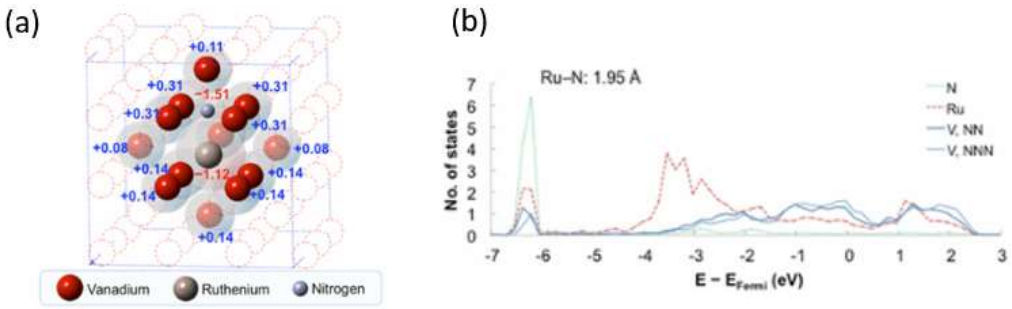

Fig. 6. Electronic effects during N binding in a $V_{53}Ru$ alloy. (a) Bader charges upon most stable N binding in $V_{53}Ru$ alloy. (b) Density of d-states projected on V, Ru and N atoms upon most stable N binding of $V_{53}Ru$ alloy. [1]

Vanadium-molybdenum case. The calculations in $V_{54-x}Ru_x$ showed that significant changes in the binding energy of interstitial N only occur when the latter "touches" an alloying atom. Ru content required to create this scenario across numerous o sites in the alloy are were presumed inaccessible with Ru. Accordingly, V_xMo_y alloys were chosen as the next study case. These alloys were studied across the whole compositional range from pure V to pure Mo. Specifically, Mo, $Mo_{15}V_1$, $Mo_{14}V_2$, $Mo_{13}V_3$, $Mo_{12}V_4$, Mo_8V_8, Mo_1V_{15}, and V were studied (Fig. 7). The lattice constants of the alloys were consistent with a linear combination of the lattice constants of Mo an V weighted by the relevant molar compositions, i.e. they closely followed Vegard's law.

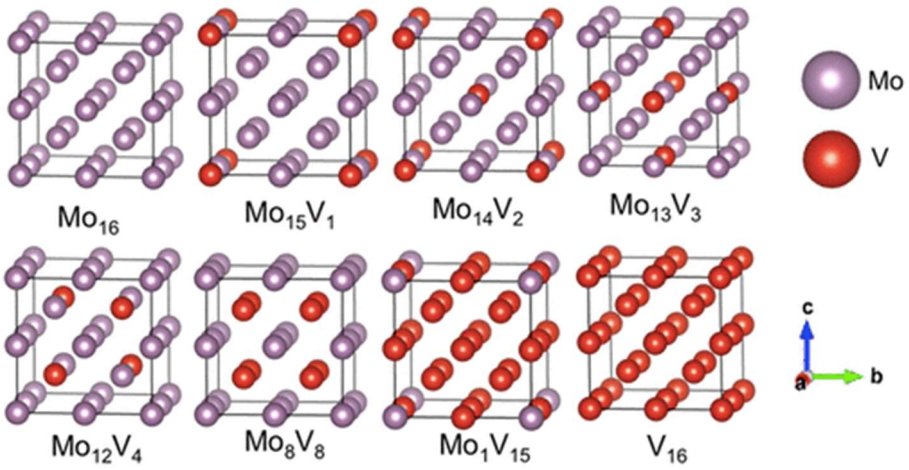

Fig. 7. Supercells illustrating the structure of studied V_xMo_y alloys [1]

Each V_xMo_y alloy presented up to five distinct *o* sites. N binding energy calculations across these *o* site for the various alloys further confirmed that N binding is primarily controlled by the composition of the local *o* site. Thus, the strongest N binding energies in each alloy were observed for *o* sites with the highest V content. The strongest N binding energy for each alloy was found to increase with overall V content (Fig. 8), because increasing the latter result in sites with higher V content. Additionally, the frequency of V-rich sites increases with overall V content as well. For instance, the fraction of *o* sites possessing binding energies stronger than -1.4 eV is 100% in Mo_1V, but 50% in Mo_8V_8.

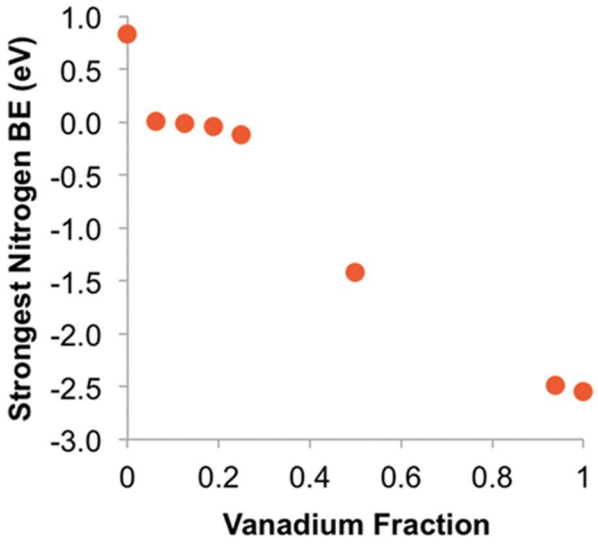

Fig. 8. Strongest N binding energy versus V content of V_xMo_y alloy. [1]

For practical application, it is ultimately desired to translate information on binding energy and binding sites to experimental observables such as nitrogen solubility. Besides general interest in this property, it directly relevant to permeability predictions in the context of nitrogen separation membranes. A first

approach to making this prediction was made using the calculated binding energy and vibrational frequencies of interstitial N to calculate relevant partition functions assuming dilute conditions are valid (see Section 2.6). The latter assumption is valid in Mo, so the prediction method was tested for this case (Fig. 9).

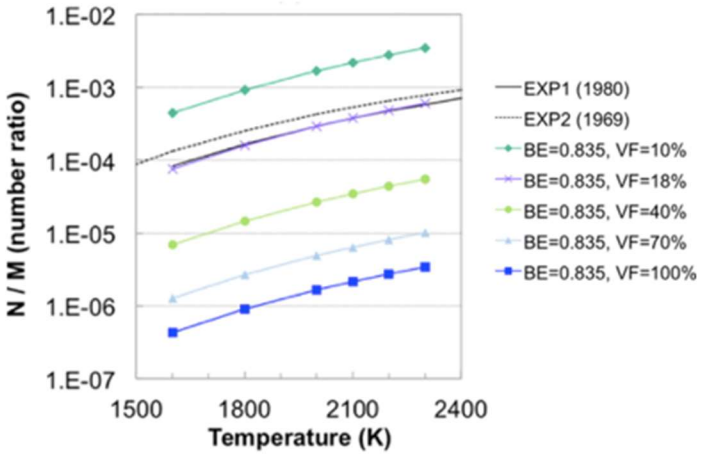

Fig. 9. Prediction of N solubility in Mo compared to experimental data. Binding energy (BE) was kept at the original calculated value, but vibrational frequencies (VF) were varied as a percentage of the original calculated values. [1]

Using "as calculated" binding energy and vibrational frequencies resulted in solubility underprediction by two orders of magnitude, although the "rate" of solubility change with temperature (which depends on ΔH_{ads}) was reasonably captured. A match to experimental solubility data was achieved when using vibrational frequencies only 18% of the "as calculated" values. This exercise boosts solubility essentially by reducing the calculated entropic loss of N during dissolution. Assuming the same frequency "scaling" works for other cases, we estimated solubilities (in the 1000-2000 K range) in the alloys relative to Mo (Fig. 10), but only for V content up to 25%. This constraint was imposed in an attempt to stay at a regime where the assumption made on Mo remain valid. Based on these predictions, varying V content in V_xMo_y alloys in the 0-25% range results in variations in solubilities spanning four orders of magnitude.

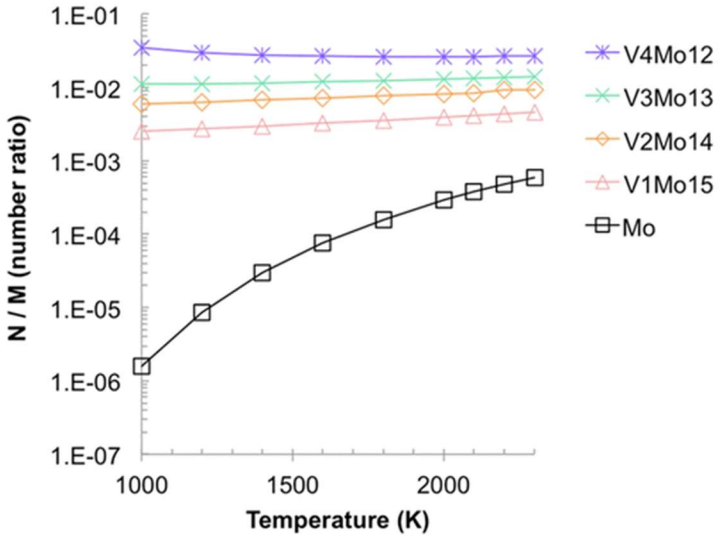

Fig. 10. Predicted N solubilities in various V_xMo_y alloy compared to prediction in Mo. [1]

3.2. Insights on the dissolution, diffusion and dissociation of nitrogen in V, V_xCr_y and V_xFe_y. This work, which follows up on work performed during Year 1, was performed during Year 3 seeking to understand nitrogen dissolution beyond the affinity of nitrogen for *o* sites in perfect BCC lattices to include other aspects influencing nitrogen dissolution such as the presence of lattice defects, dissociation at the alloy surface, and diffusion across lattice sites. Furthermore, the influence of nitrogen dissolution on alloy mechanical properties was studied as well. The alloying elements were changed from Ru and Mo to Cr and Fe due to synthetic challenges for V_xRu_y and V_xMo_y alloys that became apparent during Year 2 of the project. Since the project aim was to investigate nitrogen dissolution in the context of nitrogen separation membranes, Cr and Fe were selected because *i)* Cr and Fe present the two highest N diffusivities among BCC metals (but poor N solubility) *ii)* Cr and Fe bind N more weakly than V, so alloying could lower the binding energy, which was hypothesized in Year 1 that would enhance solubility, *iii)* V_xCr_y and V_xFe_y alloys are known to exist over a wide composition range.

Alloy properties. The composition ($V_{0.75}M_{0.25}$, $V_{0.50}M_{0.50}$, $V_{0.25}M_{0.75}$) and structure of the studied alloys (Fig. 11) guaranteed there were numerous binding sites for interstitial N that would interact directly with the alloying element. Toward the calculation of N solubility, only *o* sites in a 16-atom supercell were interrogated, because it was clear from work in Year 1 that *t* sites were less stable. In the alloys, two types of *o* sites emerged based on their local composition. The V-rich sites were designated as *o1*, and the V-poor sites as *o2*. The lattice constants and cohesive energies of V alloys were smaller than for V and reasonably well predicted by composition-weighted linear combination of the properties of the pure metals. Intermetallic V-M interactions in the alloys tend to shift the d-band center of these atoms. In the alloys, the d-band center of V, Cr and Fe tends to shift down, up and down, respectively, compared to the pure metal values.

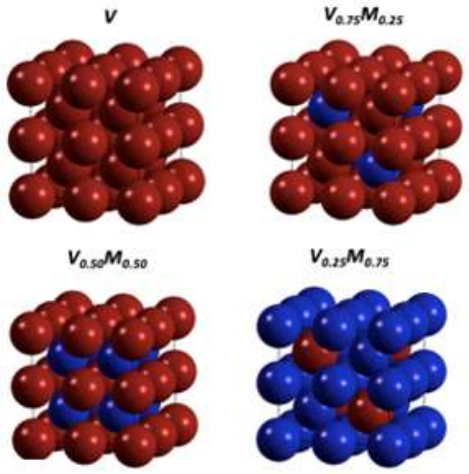

System	*a*/Å	E_{coh} /eV.at^{-1}	ε_d /eV
V	3.00	5.37	-0.25
Cr	2.85	4.05	-0.92
Fe	2.83	4.92	-1.07
$V_{0.75}Cr_{0.25}$	2.95(-0.2%)	5.07(+0.01%)	**-0.38/-0.27**
$V_{0.50}Cr_{0.50}$	2.91 (-0.3%)	4.79(+0.02%)	**-0.32/-0.46**
$V_{0.25}Cr_{0.75}$	2.88(-0.2%)	4.45(+0.02%)	**-1.21/-0.99**
$V_{0.75}Fe_{0.25}$	2.92 (-1.4%)	5.41(+2.9%)	**-0.42/-1.01**
$V_{0.50}Fe_{0.50}$	2.86 (-1.7%)	5.27(+2.4%)	**-0.57/-1.22**
$V_{0.25}Fe_{0.75}$	2.81 (-2.2%)	5.15(+2.3%)	**-0.11/-1.20**

Fig. 11. Structure, lattice constant (*a*), cohesive energy (E_{coh}) and d-band centers (ε_d) of V and V alloys. Numbers in parenthesis are deviations with respect to composition-weighted linear combination of the properties of pure metals. d-band center are reported separately (V/M) for each metal in the alloy.[3]

Binding of single interstitial N. The strength of binding energies for a single interstitial N atom (Fig. 12) were consistent with reported solubilities for the pure metals (V > Fe > Cr). Also consistent with the studies on Year 1 for alloys with Mo and Ru, the N binding energy was primarily controlled by the local environment at the *o* site. Sites that had higher content of V presented stronger N binding energies. Upon binding, the N atom was reduced as indicated by a negative electronic charge. However, contrary to the studies on V-Ru alloys in Year 1, there was no clear correlation between binding energy and N reduction (probably because Cr and Fe electronegativity values are closer to V than that the Ru V is). However, a correlation ($R^2 \sim 0.77$) was found between binding energy and a simple average of the d-band center of the atoms making up the *o* site occupied by N (Fig. 12). Notably, the d-band centers used to calculate the average were -0.25 eV, -0.92 eV and -1.07 eV, which are the values for pure V, Cr and Fe, instead of the values for the metal in the alloys as doing the latter resulted in a poorer correlation. Depending on the alloy composition, the binding energy spanned values in the -2.20 eV to 0.35 eV range (compared to -2.56 eV for V). Although pure Cr binds N more weakly than pure Fe, V_xCr_y alloys tended to bind N more strongly than V_xFe_y alloys.

System	$E_{binding}$/eV		q_N/e	
	site *o1*	site *o2*	site *o1*	site *o2*
V	-2.56 $^{(6,0)}$	-	-1.68	-
Cr	0.25$^{(0,6)}$	-	-1.56	-
Fe	-0.20$^{(0,6)}$		-1.33	-
$V_{0.75}Cr_{0.25}$	-2.20$^{(5,1)}$	-1.54$^{(4,2)}$	-1.67	-1.62
$V_{0.50}Cr_{0.50}$	-1.68$^{(4,2)}$	-0.55$^{(2,4)}$	-1.57	-1.56
$V_{0.25}Cr_{0.75}$	-0.59$^{(2,4)}$	0.35$^{(1,5)}$	-1.57	-1.50
$V_{0.75}Fe_{0.25}$	-1.21$^{(5,1)}$	0.02$^{(4,2)}$	-1.54	-1.51
$V_{0.50}Fe_{0.50}$	-1.58$^{(4,2)}$	0.13$^{(2,4)}$	-1.73	-1.51
$V_{0.25}Fe_{0.75}$	-0.51$^{(2,4)}$	0.06$^{(1,5)}$	-1.35	-1.42

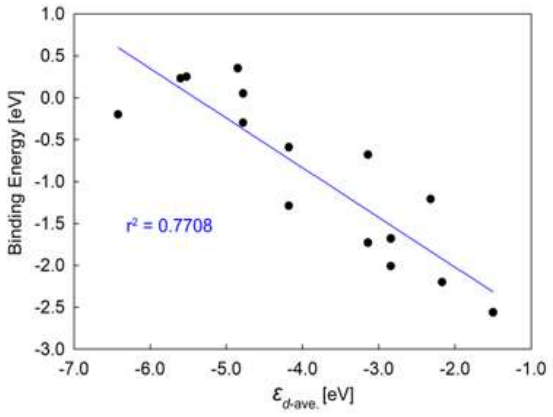

Fig. 12. Binding energies and electronic charges of interstitial N in V and V alloys, along correlation with average d-band center at local binding site. *(v,m)* superscript on binding energy indicates number of V and M atoms making up the binding site. [3]

Vacancy formation. An aspect that was not studied in alloys explored in Year 1 was how vacancy formation would affect the introduction of N into the lattice, or conversely whether the introduction of N into the lattice would facilitate the formation of vacancies. Thus, we interrogated this by removing metal atoms from the supercell and calculating the energy penalty, and by interrogating the binding of N at the formed vacancies (Fig. 13). We found that formation of vacancies tend to be easier by removing a Fe/Cr atom instead of V. Contrary to the V_xFe_y alloys, all studied V_xCr_y alloys presented less favorable vacancy formation energies than pure V. The formed vacancies did not present significant local deformations, unless N was introduced to the vacancy (Fig. 13a-c). Consistent with our earlier observations that V-rich *o* sites bind N more strongly, vacancies formed by removing Fe/Cr tend to bind N more strongly. However, while in pure V the binding of N to a vacancy more than compensates the penalty to form the vacancy, this is not case in the alloys. Accordingly, alloys are likely less prone to vacancy formation than pure V, when under a nitrogen environment. Furthermore, binding of N at the vacancies was not necessarily stronger than at regular o sites, hence indicating that vacancies may not act as nitrogen "traps."

System	E_v/eV		$E_{binding@vac}$/eV	
	V_{vac}	M_{vac}	V_{vac}	M_{vac}
V	$2.72^{(8,0)}$	-	$-2.85^{(7,0)}$	-
$V_{0.75}Cr_{0.25}$	$2.78^{(8,0)}$	$3.39^{(8,0)}$	$-1.74^{(6,1)}$	$-1.92^{(7,0)}$
$V_{0.50}Cr_{0.50}$	$3.47^{(0,8)}$	$2.94^{(8,0)}$	$-1.51^{(3,4)}$	$-1.53^{(4,3)}$
$V_{0.25}Cr_{0.75}$	$2.96^{(0,8)}$	$2.81^{(4,4)}$	$0.34^{(0,8)}$	$-0.77^{(3,4)}$
$V_{0.75}Fe_{0.25}$	$2.97^{(8,0)}$	$1.67^{(8,0)}$	$0.39^{(5,1)}$	$-0.23^{(7,0)}$
$V_{0.50}Fe_{0.50}$	$1.85^{(0,8)}$	$1.10^{(8,0)}$	$0.20^{(3,4)}$	$0.09^{(4,1)}$
$V_{0.25}Fe_{0.75}$	$2.75^{(0,8)}$	$3.01^{(4,4)}$	$-1.33^{(0,4)}$	$-1.70^{(3,1)}$

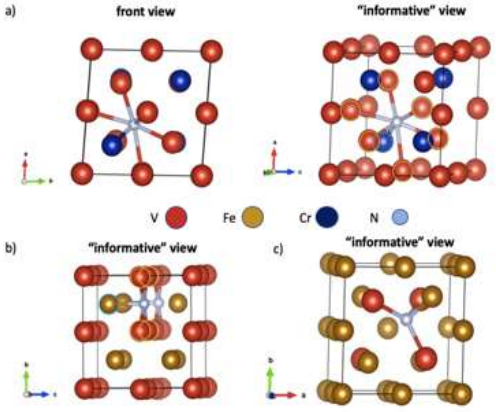

Fig. 13. Vacancy formation energies and N binding energies at vacancies, along with example configurations. *(v,m)* superscript on binding energy indicates number of V and M atoms around the vacancy. Configurations show (a) Seven-neighbor N binding at vacancy in $V_{0.75}Cr_{0.25}$. N atom is at the center of the base of a (distorted) hexagonal pyramid. (b) Five-neighbor N binding at vacancy in $V_{0.50}Fe_{0.50}$. N atom is at the center of the base of a square pyramid. (c) Five-neighbor N binding at vacancy in $V_{0.25}Fe_{0.75}$ case. N atom is at the center of a distorted tetrahedron. [3]

Loading effects during insertion of multiple interstitial N. Analogous to how "coverage" is known to affect binding energetics on surfaces, binding energetics at interstitial sites can also vary as the lattice loading changes. It was important to understand N diffusion in the lattice, because as atomic N permeates, numerous interstitial sites can become occupied. The studied supercells 16 metal atoms and 48 *o* sites (24 *o1* and *o2* sites, respectively), and were loaded with up to 16 N atoms. For each loading, we aimed to identify the most stable binding configuration. This was ensured by brute force search for up to three atoms.

After that, the number of configurations interrogated for each loading was kept tractable by using heuristic stability principles emerging from the low-loading calculations. We plotted the average binding energy versus loading (Fig. 14-left), which revealed significant "loading effects."

Due to "loading" effects, the average binding energy was found to vary anywhere between 0.6 eV and 2.0 eV (data that is relevant for multiscale modeling of N diffusion in the alloy lattice) as loading changed. The binding energy for early addition of N to the lattice generally strengthened with each subsequent addition up to three or four N atoms. This increase in favorability was 0.4 eV for pure V and 0.3 – 0.8 eV for the alloys. After this point, each subsequent addition tends to be associated with weakest binding energy than the preceding one. For pure V, $V_{0.75}Fe_{0.25}$ and $V_{0.50}Cr_{0.50}$, the average binding energy ended up (by the 16th N addition) significantly less favorable than for the binding of the first interstitial N atom, but for the remaining alloys, the average binding energies remained similar or below to that for the first N binding.

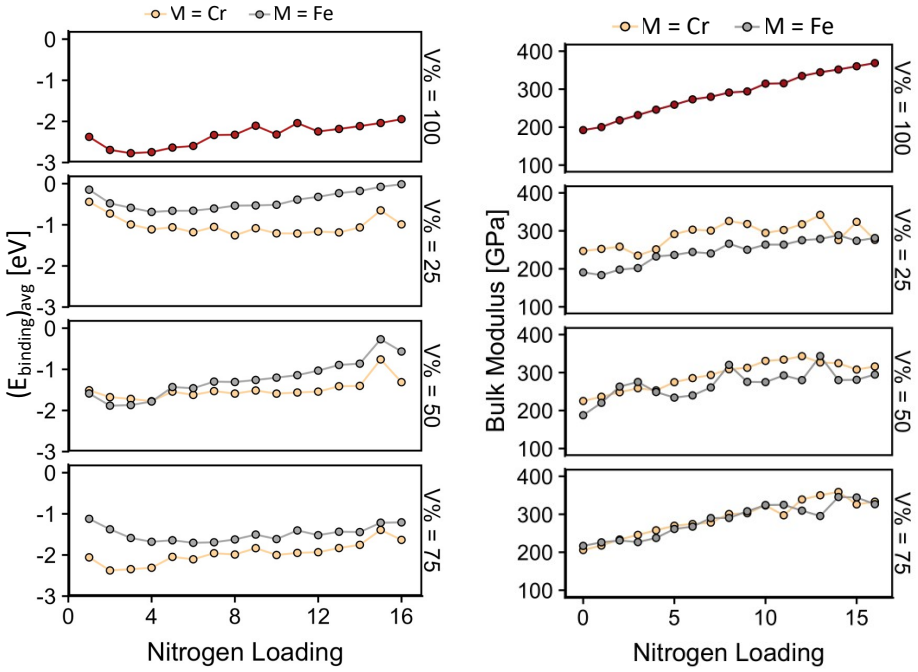

Fig. 14. Average binding energy and bulk modulus for V and V alloys as nitrogen fills the lattice. Left: Average binding energy versus N loading. Right: Bulk modulus versus N loading. [3]

Some common observations as the lattice fills with interstitial N are *i)* regardless of loading effects, the *o1*-type (i.e. V-rich) sites bind N atoms more strongly (i.e. the lattice fills by occupying *o1*-type sites). *ii)* regardless of binding energy variations due to loading, the composition-based trends obtained with the first binding remain (e.g. N binds more weakly as V content in the alloy decreases, and V_xCr_y alloys bind N more strongly than V_xFe_y alloys), *iii)* As the lattice fills, N first occupies the eight *o1*-type sites that have the same orientation, and after that they start occupying *o1*-type sites of a different orientation, *iv)* As the lattice fills, both the coordination of interstitial N with V atoms and distances between interstit ial N remain as large as possible, *v)* For the first eight N atoms, the lattice only expands in two directions, which results in a lower average metal-metal distance than if expansion occurred in three directions

Evolution of mechanical properties with increase in N content. Change in mechanical properties with increase in N content is relevant to common nitriding processes, but also critical for nitrogen separation membranes, which should remain mechanically stable (e.g. no cracks) to maintain the expected selectivity. Thus, we evaluated the change in mechanical properties as a function of composition during the sequential N loading (Fig. 14-right). The addition of smaller quantities of Fe or Cr to V seems to increase the baseline bulk modulus *K*. Specifically, $V_{0.75}Cr_{0.25}$ and $V_{0.75}Fe_{0.25}$ present *K* values 14 GPa and 24 GPa, respectively, higher than V. More significant increases in M content presented varied effect between Fe and Cr. Intriguingly, although Fe has a larger *K* than V while Cr has a smaller *K*, is the introduction of significant iron content that reduces the *K* of V. Consistent with the hardening typically associated with nitriding, the *K* increases with *N* content. For V, the increase is more monotonic, with *K* increasing almost two-fold by the time of the 16^{th} N addition. For the alloys, the increase in bulk modulus is both more irregular and less pronounced as the V content in the alloy decreases. Again surprising, due to the larger *K* of Fe than Cr, considering all N loadings, higher bulk moduli are generally found for V_xCr_y alloys than for V_xFe_y.

N solubility and nitride formation. The approach used in Year 1 to calculate N solubility was better suited for cases where dilute conditions are applicable such as with Mo-rich V_xMo_y alloys. However, Cr and Fe present higher affinities for N than Mo, and the V_xCr_y and V_xFe_y compositions studied here present a much higher V content. Thus, in Year 3, we used ab-initio thermodynamics (AT) to calculate N solubility because dilute conditions are arguably inadequate while it is also necessary to consider the formation of nitride as a possibility. The obtained phase/solubility diagrams are shown in Fig .15, with relevant operating conditions (to nitrogen separation) enclosed by the blue box. According to AT, at these conditions, V is predicted to dissolve 16 N atoms, transforming into the rock-salt VN nitride structure.

Our calculations indicate that only until Cr content increases beyond 75%, nitride would not form during membrane operation. With 75% Cr content, a ~25% reduction in solubility relative to pure V is predicted. On the other hand, nitride formation is not anticipated in the alloys with Fe, although at the expense of more pronounced shifts in N solubility. At the relevant operation conditions, 25% and 50% Fe content already present a ~13% and ~31% reduction in solubility, respectively, relative to V, while for 75% content the reduction is ~69% (~3-fold). Notably, although N solubilities are expected to go down due to alloying, they are also expected to remain within the same order of magnitude as for pure V.

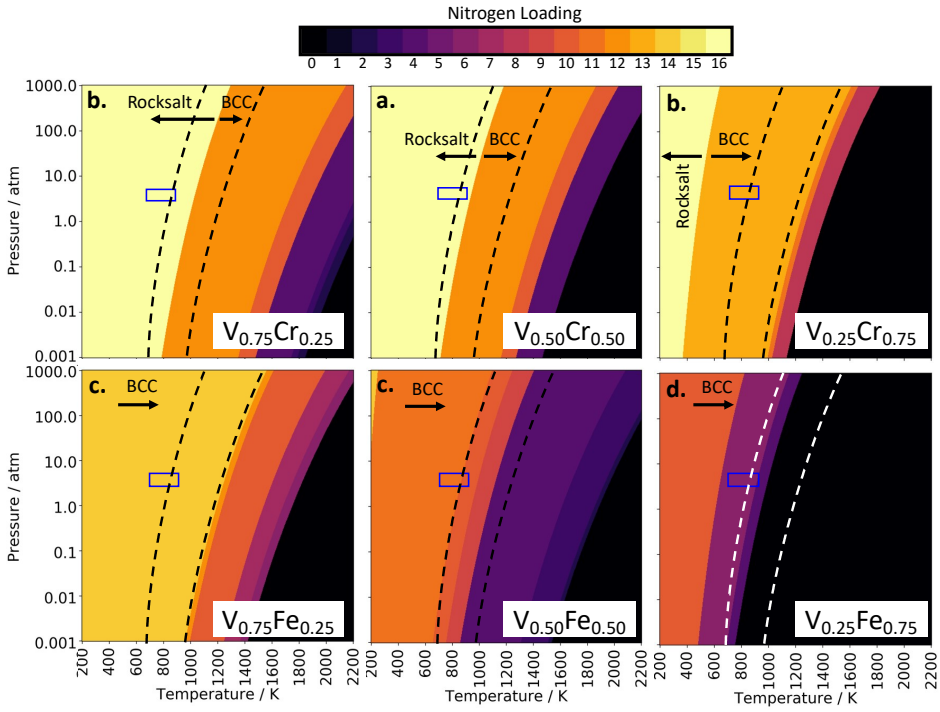

Fig. 15. Phase/solubility diagrams for V alloys in the presence of a nitrogen atmosphere. As reference, dashed lines indicate boundaries for pure V. [3]

N diffusion and permeability. The next aspect of nitrogen transport through the metal lattice that we studied was the barrier for N hopping from one lattice site to another. Thus, we calculated the minimum energy path (MEP) for N to hop from an *o1* to an *o2* site (Fig. 16). Two different kind of *o2* sites (different orientation) can be reached from an *o1* site, giving rise to two possible paths, *p1* and *p2*. The easiest diffusion path was p_1, where N hop from *o1* to *o2* through a transition state corresponding to the N atom in a *t* site. As reference, the barriers for N hopping in V, Cr, and Fe were calculated as 1.24 eV, 1.15 eV and 0.85 eV, respectively, consistently with trends in measured diffusion coefficients.

Contrary to the pure metals, in the alloys, the MEP are nonsymmetric due to the energetic disparity between the V-rich *o1* site and the V-poor *o2* sites. This disparity generally ended up producing higher N hopping barriers in the alloys than in V. For instance, $V_{0.50}Fe_{0.50}$ presented the highest barrier (2.09 eV) due to the largest disparity between binding at the *o1* and *o2* site (-1.58 eV vs. 0.13 eV). The one exception was $V_{0.25}Fe_{0.75}$, which did present a lower hopping barrier than pure V (1.01 eV vs. 1.24 eV), which—assuming similar frequency factor—indicates a hopping ~7,758, ~53, and ~21 times faster in the alloy at 298 K, 673 K, and 873 K, respectively, based on the Arrhenius equation. Based on the predicted relative N solubility in $V_{0.25}Fe_{0.75}$ with respect to V, the relative hopping rates above indicate that the N permeability of $V_{0.25}Fe_{0.75}$ at 673 K and 873 K would be expected to be ~20 and ~5 times higher than for pure V—assuming V does not turn into nitride, in which case the differences would be dramatically higher.

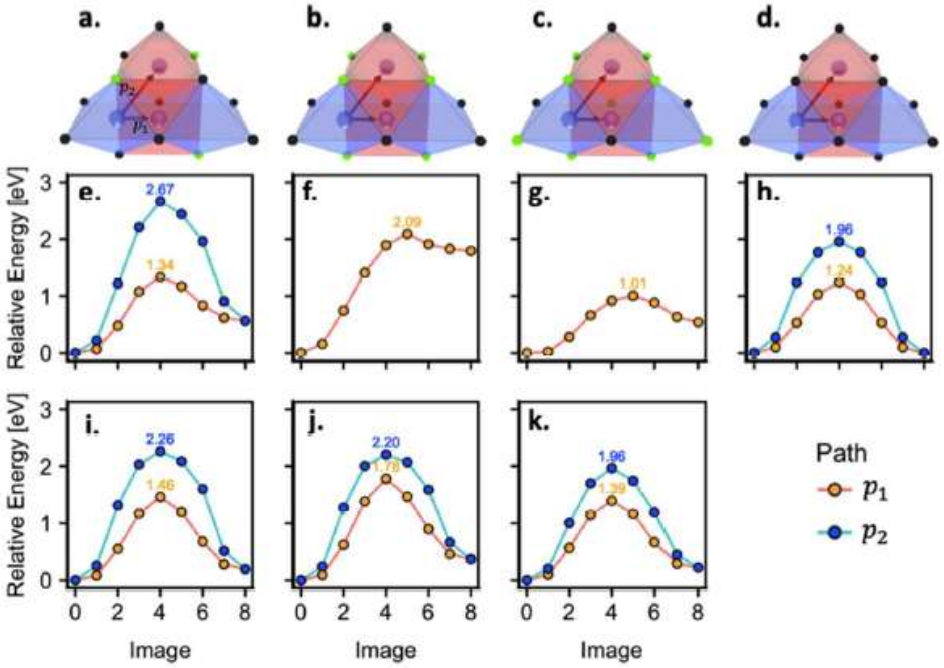

Fig.16. Energy barriers for N hopping from an *o1* site to an *o2* site in V and V alloys. Numbers indicate the energy barrier for the hop. Hopping path in (a) $V_{0.75}M_{0.25}$ (b) $V_{0.5}M_{0.5}$, (c) $V_{0.25}M_{0.75}$, (d) V. Minimum energy paths in (e) $V_{0.75}Fe_{0.25}$ (f) $V_{0.5}Fe_{0.5}$ (g) $V_{0.25}Fe_{0.75,}$ (h) V, (i) $V_{0.75}Cr_{0.25}$ (j) $V_{0.5}Cr_{0.5}$ (k) $V_{0.25}Cr_{0.75,}$ [3]

Nitrogen dissociation. The energetics of N_2 dissociation on the surfaces of the alloys was calculated (Fig. 17) to interrogate whether N permeation was controlled by surface or bulk processes. If permeation was controlled by bulk processes, then the predicted improvements in N permeability in $V_{0.25}Fe_{0.75}$ relative to V previously predicted should be expected to be detected experimentally. The initial state (IS) for the dissociation reaction corresponded to non-dissociative adsorption of the N_2 molecule, with the final state (FS) corresponding to the dissociated state. The transition state (TS) connecting the non-dissociated and dissociated state presented different levels of "earliness" depending on alloy composition.

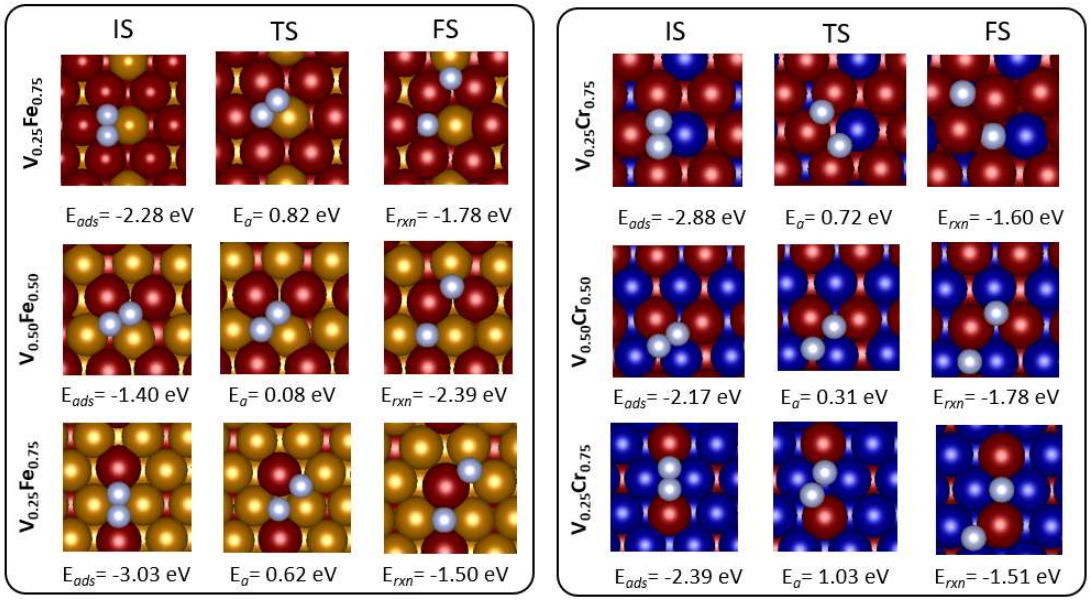

Fig. 17. Adsorption and dissociation of N_2 on alloy surfaces. The initial state (IS) corresponds to the adsorption of N_2 (with adsorption energy E_{ads}). The final state (FS) corresponds to the dissociated N2 (with reaction energy E_{rxn}). The transition state (TS) is illustrated along with the corresponding activation energy (E_a).[3]

We found that N_2 binding in V alloys with Cr was stronger than in alloys with Fe, except for $V_{0.25}Cr_{0.75}$ and $V_{0.25}Fe_{0.75}$. Contrary to the binding of interstitial N, we did not find an as clear correlation between adsorption energy E_{ads} and the amount of coordinating V in the adsorption site. Although roughly, reaction and activation energies are linearly correlated ($R^2 \sim 0.64$) as expected from the Brønsted-Evans-Polanyi (BEP) principle (Fig. 18). Deviations are likely due to geometric dissimilarities for the dissociation path in the different alloys when considering, for example, the varied "earliness" of the transition states (as evidenced by the corresponding N-N distance). Notably, the relationship with transition state "earliness" and V content in the alloys was inverse between alloys with Cr and Fe. For alloys with Cr, the lateness of the TS increases with V content, while the opposite was observed for alloys with Fe. Relevant to membrane applications, the barrier for surface dissociation of N_2 into atomic N is in all instances lower than the corresponding barrier for bulk diffusion in the alloy. Thus, N diffusivity is expected to be controlled by the latter, with the relative N diffusivities between alloys corresponding to the ratios described in the previous subsection.

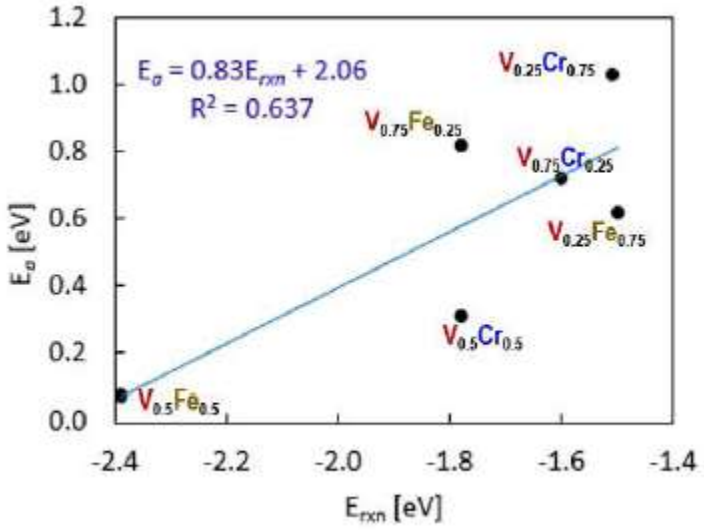

Fig. 18. Correlation between reaction (E_{rxn}) and activation energies (E_a) for N_2 dissociation on V alloys. [3]

3.3. Insights on the link between hydrogen dissolution and mechanical properties of Pd, Pd_xAu_y and Pd_xAg_y. This work was performed during Year 2 and (first half of) Year 3, seeking to shed light on how the dissolution of hydrogen in Pd and Pd alloys impact material properties, and potentially reveal connections to hydrogen embrittlement (HE). HE is one of the fundamental challenges in material science, but it is not fully understood, which hinders rational design of HE-resistant materials. In the context of hydrogen separation membranes, Pd offers practical permeabilities but it is susceptible to HE-induced failure. Thus, materials that are HE-resistant but present practical permeabilities are desired. On the other hand, improvements in HE-resistance have been observed in Pd alloys with Au or Ag, but the reasons for the improvement are not well understood. Accordingly, Pd, Pd_3Au, Pd_2Au_2, $PdAu_3$, Pd_3Ag, Pd_2Ag_2 and $PdAg_3$ were selected as study cases, for which the binding of hydrogen in perfect and defected lattices was interrogated at various loadings and loading sequences, while tracking associated deformations and changes in mechanical properties.

Binding of interstitial H atoms. At the beginning of this work both tetrahedral (*t*) and octahedral (*o*) sites in the FCC lattice (Fig. 19) of Pd and Pd alloys were interrogated. The lattice constants of the alloys were reasonably predicted (< 1% absolute error) using Vegard's law. Since Ag (Au) is less (more) electronegative than Pd, Ag (Au) atoms in the alloy lattice were found to lose (gain) electron density. Au and Ag are known to bind H more weakly than Pd. Therefore, a noteworthy observation was that Pd_3Au and Pd_3Ag alloys presented some interstitial sites binding H more strongly than in Pd (Table 1 (n = 1)).

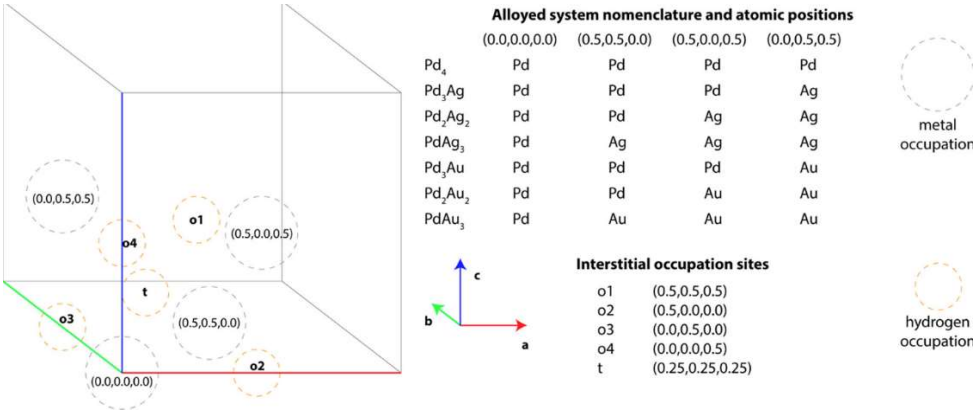

Fig. 19. Occupation of lattice sites in Pd and Pd alloys and interrogated interstitial sites for H binding. [2]

Interrogation of sequential H binding (Table 1) showed that while the strongest binding site in Pd_3Au and Pd_3Ag alloys binds H more strongly than in Pd (-0.27 eV and -0.34 eV versus -0.25 eV), their remaining interstitial sites in the lattice bind H significantly more weakly. While Pd can occupy interstitial sites with relatively similar H binding strength up to the point where the M:H ratio (M = metal) is one, occupation of interstitial sites in Pd_3Au and Pd_3Ag alloys after an M:H ratio of 0.25 presents an H binding 0.36 eV weaker on average. Indeed, the lower number of "strong" H binding sites in Pd_3Au and Pd_3Ag is expected to lower their hydrogen solubility relative to Pd. For Pd_2Au_2, Pd_2Ag_2, $PdAu_3$ and $PdAg_3$ H binding at all M:H ratios is weaker than Pd, so evidently they are expected to present lower hydrogen solubility as well.

Table 1. Site preference and binding energies (eV) as H sequentially fills interstitial sites in Pd and Pd alloys. [2]

	Dissolution step *n*				
System	*n* = 1	*n* = 2	*n* = 3	*n* = 4	*n* = 5
Pd_4	-0.25(*o2*)	-0.26(*o4*)	-0.26(*o3*)	-0.21(*o1*)	0.45(*t*)
Pd_3Ag	-0.34(*o2*)	0.02(*t*)	0.11(*o3*)	-0.10(*o4*)	0.52(*o1*)
Pd_2Ag_2	-0.16(*o2*)	-0.17(*o4*)	0.63(*t*)	0.67(*o1*)	0.40(*o3*)
$PdAg_3$	0.14(*o2*)	0.57(*o4*)	0.49(*o3*)	0.31(*t*)	0.48(*o1*)
Pd_3Au	-0.27(*t*)	0.09(*o2*)	0.17(*o4*)	0.06(*o3*)	0.92(*o1*)
Pd_2Au_2	-0.01(*o4*)	0.03(*o2*)	0.60(*t*)	0.54(*o1*)	0.24(*o3*)
$PdAu_3$	0.39(*o4*)	0.79(*o2*)	0.52(*o3*)	-0.05(*t*)	0.49(*o1*)

There was some correlation (R^2 ~0.72) between binding energies and lattice volumes. However, we concluded this was reflection of the inherent affinity for H happening to follow the reverse order of atom size (Au > Ag > Pd). On the other hand, we were able to obtain a stronger correlation (R^2 ~ 0.92) between binding energy and electronic features of the studied materials. Specifically, between binding energy and the corrected d-band center, ε'_d, at the local interstitial site (Fig. 20). The value of ε'_d is calculated as:

$$\varepsilon'_d = \sum_j e^{\frac{-r_{ij}}{r_{0,j}}} \times \varepsilon_{d,j} V_j$$

where the index j runs over each metal atom making up the interstitial site. Thus, V_j and $\varepsilon_{d,j}$ are the coupling matrix element and d-band center of each metal atom j, and the exponential factor is a correction factor that depends on what is the distance between H and metal atom j at the interstitial site (r_{ij}) relative to the metal

Van der Waals radius $r_{o,j}$. That the d-band center influences H binding is consistent with *d*-band theory, while the exponential term accounts for the extent of Pauli repulsion felt by the binding H.

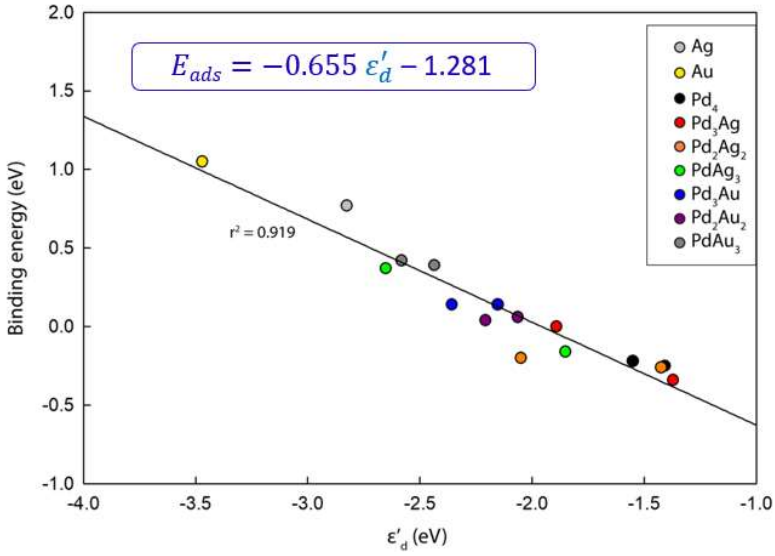

Fig. 20. Correlation between H binding energy in Pd and Pd alloys and corrected local d-band center. [2]

Relationship between H binding and vacancy formation. Lattice vacancies are generally mentioned among the culprits for the occurrence of HE. Often in the context of vacancy diffusion and agglomeration into supervacancies. Accordingly, we interrogated the energy penalty, E_v, to form a "mono-vacancy" by removing a single metal atom from the supercell. We considered two scenarios in which the presence of hydrogen could promote vacancy formation: *i)* the presence of H in regular interstitial sites makes the removal of a metal atom easier, *ii)* a vacancy created by the removal of a metal atom is stabilized by the diffusion of H to the vacancy and subsequent binding. To examine the first scenario, we simply removed either a Pd or an Au/Ag atom from the pristine system (M:H = ∞) and the "hydride" system (M:H = 1). Removal of Pd was found to be easier than Au/Ag. A clear observation was that the presence of hydrogen in the lattice did make the formation of the vacancy easier in all systems (Table 2). However, considering that the alloying with Au or Ag is experimentally reported to improve HE-resistance in Pd, an intriguing finding was that the penalty to form vacancies was less in the Pd alloys.

Table 2. Vacancy formation energy in "pristine" and "hydride" Pd and Pd alloy systems

System	*Ev* (eV) *M:H* = ∞		*Ev* (eV) *M:H* = 1	
	-Pd	*-X*[a]	*-Pd*	*-X*[a]
Pd_4	1.20	---	0.31	---
Pd_3Ag	1.04	1.32	-0.25	-0.27
Pd_2Ag_2	0.65	0.93	-1.32	-1.06
$PdAg_3$	0.96	0.94	-1.18	-0.82
Pd_3Au	0.99	1.40	-0.37	-0.62
Pd_2Au_2	0.89	1.37	-0.40	-0.58
$PdAu_3$	0.73	0.86	0.06	0.00

[a] X is either a Ag or Au atom

To examine the second scenario for vacancy stabilization, we interrogated the binding of H atom upon vacancy formation (Fig. 21). This exercise produced another intriguing result in that it was in Pd_3Au and Pd_3Ag where the binding of H at the vacancy was strong enough (-1.24 eV and -1.06 eV in Pd_3Ag and Pd_3Au, respectively) to compensate for the penalty to form the vacancy (1.04 eV and 0.99 eV in Pd_3Ag and Pd_3Au, respectively). In contrast, the binding of H at the vacancy in Pd (-0.20 eV) was not enough to compensate the vacancy formation penalty (1.20 eV). Although a distinctive feature of vacancies in Pd is that they can accommodate up to 6 H atoms, keeping an average binding energy of -0.05 eV, this is still far from compensating the removal of a Pd atom.

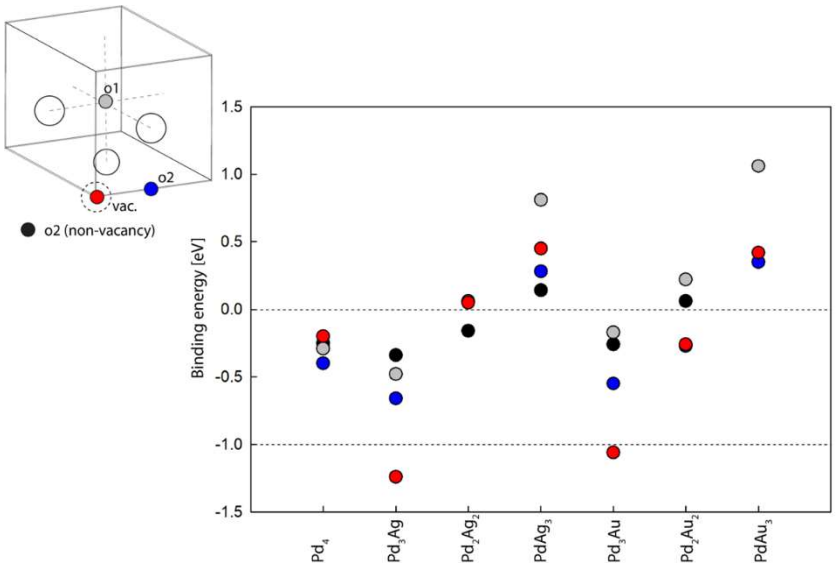

Fig. 21. Binding energy of H at various sites in defected (with vacancies) Pd and Pd alloy lattices. [2]

Deformation during H loading/unloading. In aiming to improve materials for hydrogen separation membranes, another factor to consider is how the material responds to hydrogen loading/unloading cycles as plastic deformation induced by these processes could be potentially linked to hydrogen-induced failure. One of our first observations during this endeavor was that the rate at which hydrogen was introduced to the lattice impacted the shape and volume of the studied supercells (Fig. 22). A fast rate, as mimicked by the simultaneous addition of four H to the supercell to "instantaneously" form a hydride, tended to result in isotropic material expansion. On the other hand, a slower rate, as mimicked by the stepwise addition of H until a hydride is formed, tended to result in pronounced anisotropic material changes. Notably, this anisotropy arised only in the Pd alloys (specially with higher Au or Ag content) but not on pure Pd.

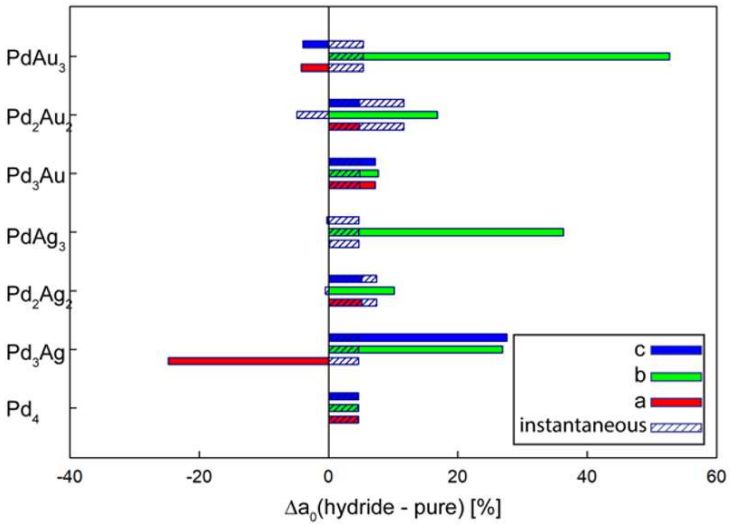

Fig. 22. Deformation of lattice constants in "hydride" relative to "pristine" system depending on the rate of loading. Hashed and solid bars are for instantaneous loading (all four H atom added simultaneously to the supercell) and stepwise loading (each H atom added one at a time followed by optimization), respectively. [2]

While during a full (stepwise) H loading/unloading cycle on pure Pd the material lattice returns to the original state, this is not the case with the alloys (Fig. 23). For instance, in Pd_3Ag, a distinct anisotropic expansion exists, predominantly along the *a* lattice vector. This deformation is permanent through one cycle as evidenced by a -30 to +25% change in lattice constants relative to the pre-absorption system. The significant differences in lattice distortion introduced by the different kinetics of loading were considered harbingers of hysteresis (changes in H solubility depending on cycling characteristics) occurring upon hydrogen unloading, which was important to examine considering that it might influence H dissolution in subsequent cycles beyond the first loading/unloading loop in the alloys.

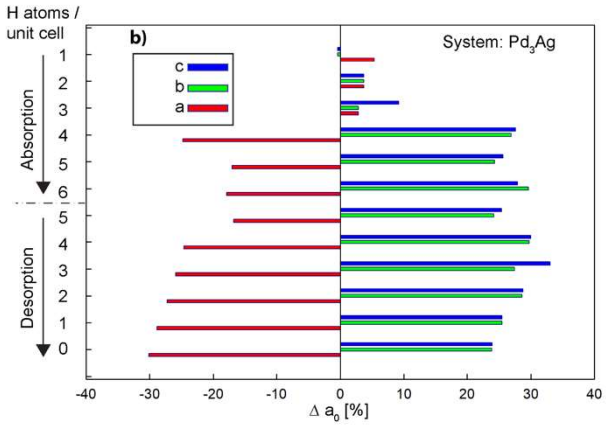

Fig. 23. Expansion and contraction in lattice constants during a H loading/unloading cycle in Pd_3Ag. [2]

Calculation of H binding energies during H loading/unloading provided further evidence to support the occurrence of hysteresis (Fig. 24). The plastic deformations during H loading/unloading change the lattice geometry across different cycles in such a way that at the same M:H ratio an added H sees a somewhat different binding environment. For instance, following up with the Pd_3Ag system, H added to the pristine lattice after a first cycle experiences a weaker binding energy than the hydrogen added to the pristine lattice before any cycling. On subsequent steps, however, the trend is inverted. Overall, it seems that an increase in ductility in the Pd alloys facilitate plastic deformations that would ultimately result in hysteresis in these alloys (but not in pure Pd).

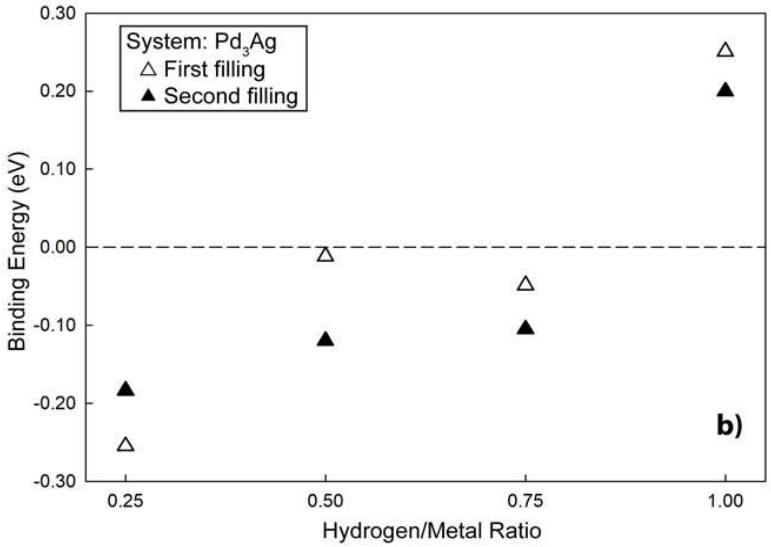

Fig. 25. H binding energies in a Pd3Ag alloy before and after a hydrogen loading/unloading cycle**.** [2]

Impact of H dissolution on mechanical properties. The tendency for ductility to increase due to alloying was confirmed by the calculation of the Pugh's ratio (bulk modulus over shear modulus) in the studied systems at various M:H ratios (Fig. 26). It is believed that an increase in Pugh's ratio beyond ~1.75 indicates a material transition from brittle to ductile. Accordingly, all systems at all hydrogen loadings can be considered ductile. However, the increase in ductility in the alloys relative to pure Pd is remarkably pronounced for hydrogen to metal ratios in the 0.5 – 0.75 range.

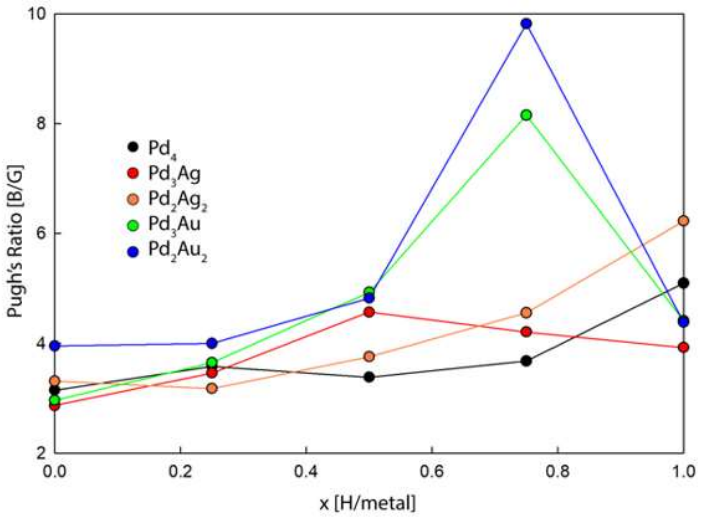

Fig. 26. Pugh's ratio calculated in Pd and alloys as a function of hydrogen to metal ratio. [2]

HE is a highly complex phenomenon whose underlying mechanism continues under debate. Proposed mechanisms include the decohesion model, the H-enhanced local plasticity (HELP), and the H-enhanced strain-induced vacancy (HESIV). By comparing the effect of H on studied properties in Pd and alloys, we postulate a tentative explanation for the apparent (experimentally observed) higher resistance of the alloys to HE. A fair comparison of calculated properties, however, must be done at similar operating conditions (e.g. temperature and hydrogen pressure) rather than at similar H loading. To this end, we applied ab-initio thermodynamics (AT) to obtain phase/solubility diagrams (Fig. 27), with particular focus on Pd_3Ag and Pd_3Au. Notice that regions calculated to have zero H solubility are likely regions in the dilute solution regime, which cannot be quantitatively described by AT as it would require intractable supercell sizes.

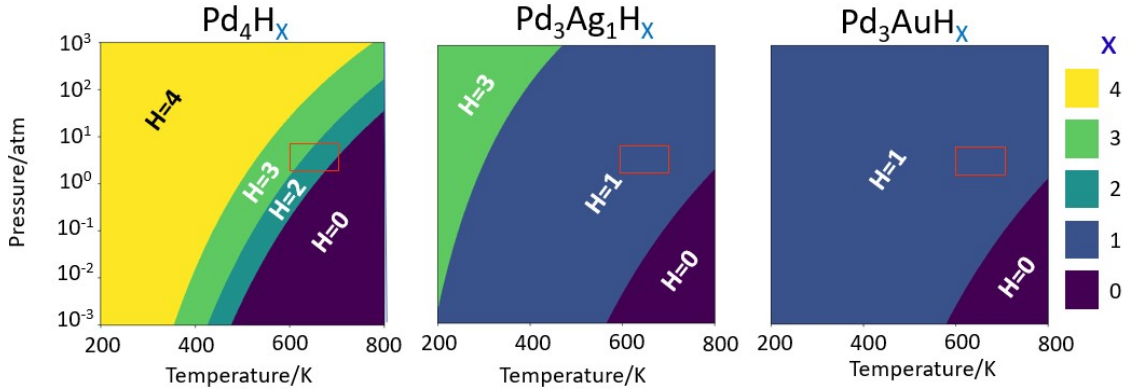

Fig. 27. Phase/solubility diagrams for hydride formation/hydrogen dissolution in Pd and Pd alloys predicted from *ab initio* thermodynamics. Typical membrane operating conditions on the retentate side are enclosed by the red box**.** [2]

Although the addition of the first H to the supercell is more stable in Pd_3Ag and Pd_3Au than in Pd, ultimately the larger number of strong binding sites in the latter results in Pd having a solubility two to three times higher than the alloys at the relevant operating conditions (600–700 K and 2–8 atm). Whereas Pd_3Ag and Pd_3Au seem to dissolve H with a 0.25 hydrogen to metal ratio, Pd does it with a ratio in the 0.5-0.75 range.

With this baseline, we proceeded to compare the calculated Pughs' ratio (Fig. 26), Young's modulus (Fig. 28) and Shear modulus (Fig. 28) at the relevant ratios

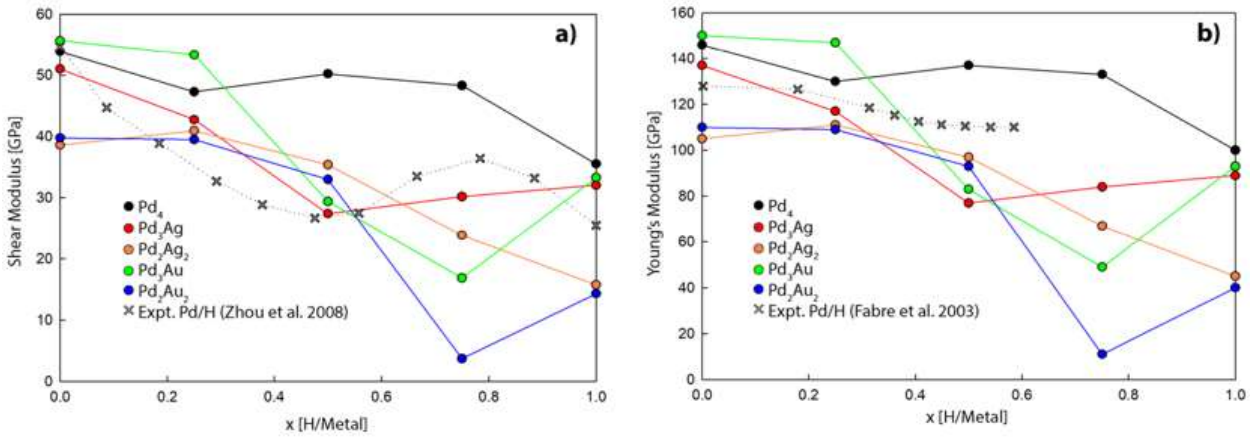

Fig. 28. Elastic properties of Pd and Pd-alloyed systems as a function of hydrogen to metal ratio. [2]

We observed that both the Young's and shear moduli follow the trend Pd_3AuH > Pd_4H3 > Pd_3AgH. As some reports have associated a decrease in elastic constants with hydrogen embrittlement failure, this would suggest Pd_3Ag to be less robust than Pd, which would contradict experimental findings. It is possible that the reported reduction in elastic constants was actually capturing an increase in ductility that may facilitate local ductile process leading to failure as in the HELP and HESIV models. From the Pugh's ratio, the ductility of Pd_4H3 is slightly higher than for Pd_3AgH and Pd_3Au. The opposite would have been observed at the same H loading. Thus, our calculations point to the difference in hydrogen solubility as the key to prevent HE.

The more pronounced H-stabilization of vacancies in Pd_3Ag and Pd_3Au than in Pd further supports that, ultimately, is the lower presence of hydrogen in the lattice what makes the alloys more resistant to HE than pure Pd. Additionally, only in pure Pd a formed vacancy can syphon up to 6 H to further boost hydrogen availability to stabilize formation of other vacancies.

IV. RECOMMENDATIONS

Based on the findings obtained through the course of this project, the following recommendations are presented for future research.

- Given the energetic heterogeneity of interstitial binding sites for nitrogen, along with strong dependence of binding energies on number and distribution of nitrogen in the lattice, it is recommended that a multiscale approach such as kinetic Monte Carlo be used to directly model macroscopic N diffusion. This will allow understanding better both diffusion in nitrogen separation membranes and early stage of nitriding processes.

- Kinetic Monte Carlo models to model macroscopic diffusion will need for fast, effective ways to predict changes in diffusion barriers due to the presence of lattice defects and changes in lattice occupation. A potential way forward is to use scaling relationships relating the energy difference between adjacent lattice sites to the energy barrier for diffusion between those sites. For effective ways to calculate the energy difference, developing cluster expansion and/or machine learning models could provide useful.

- Ab-initio thermodynamics was found useful to evaluate the stability of nitrides, and in turn the tendency for their formation in V and V alloys. However, only one nitride composition/structure (rocksalt, MN) was considered. As other metals can form other nitrides, future studies should consider more possibilities for nitride composition/structure that could potentially form.

- It was possible to find some correlations between N and H binding and properties of the lattice. However, for different adsorbates and metal systems the correlations were with different properties. This suggests that there could be a fundamental, but more general connection between chemistry and geometric and electronic structure of binding sites and binding energies. It could be possible to gain further fundamental insights on the binding of atomic species in metal lattices from the analysis of large amounts of data generated by simulation and subsequently trained machine learning models.

V. PERSONNEL

The following is a list of individuals who have worked on this project under the full or partial support by the Air Force Office of Scientific Research under Grant FA9550-16-1-0357

Year 3

- Prof. Diego A. Gomez-Gualdron: Assistant Professor, Department of Chemical and Biological Engineering, Colorado School of Mines.
- Dr. Peter Psarras: Research Associate, Department of Chemical and Biological Engineering, Colorado School of Mines.
- Mr. Ryther Anderson: Graduate student (Ph.D. in progress) Department of Chemical and Biological Engineering, Colorado School of Mines.

Year 2

- Prof. Jennifer Wilcox[a], Associate Professor, Department of Chemical and Biological Engineering, Colorado School of Mines.
- Dr. Peter Psarras: Postdoctoral Fellow, Department of Chemical and Biological Engineering, Colorado School of Mines.

Year 1

- Prof. Jennifer Wilcox[a], Associate Professor, Department of Chemical and Biological Engineering, Colorado School of Mines.
- Dr. Peter Psarras: Postdoctoral Fellow, Department of Chemical and Biological Engineering, Colorado School of Mines.

[a] At the end of Year 2, Prof. Wilcox moved to Worcester Polytechnique Institute (WPI) as the James H Manning Chaired Professor at the Department of Chemical Engineering.

IV. PUBLICATIONS

The following is a list of publications resulting from this project, wholly or partially supported by the Air Force Office of Scientific Research under Grant FA9550-16-1-0357

[1] Kyoungjin Lee, Simona Liguori, Peter Psarras and Jennifer Wilcox, Theoretical Study of Nitrogen Absorption in Metals, *J. Phys. Chem. C* (**2017**), 121, pp 17016-17028, doi.org/10.1021/acs.jpcc.7b05315

[2] Peter Psarras, Ryther Anderson, Diego A. Gomez-Gualdron and Jennifer Wilcox, Material Consequences of Hydrogen Dissolution in Palladium Alloys Observed from First Principles, *J. Phys. Chem. C* (**2019**), 123, pp 22158-22171, doi.org/10.1021/acs.jpcc.9b03685

[3] Peter Psarras, Ryther Anderson, Jennifer Wilcox and Diego A. Gomez-Gualdron, Dissociation, dissolution and diffusion of nitrogen on V_xFe_y and V_xCr_y alloy membranes studied by first principles, *J. Phys. Chem. C* (**2019**), *under review*